Journal of Systems Engineering and Electronics (ISSN NO: 1671-1793) Volume 35 ISSUE 9 2025

Hydrothermal Synthesis of Gd-Doped Fe_3O_4 @ $NaYF_4$ Core-Shell Nanostructures: A Dual-Functional Material for supercapacitor and Photocatalytic Applications

J.Ragavidurga *, T.Sumathi and C.Rakkappan

Department of Physics, Annamalai University, Annamalainagar, Chidhambram-608002, Tamilnadu, India

Abstract

In this work, Fe_3O_4:Gd@$NaYF_4$ core-shell nanoparticles were successfully synthesized via a facile hydrothermal method. Structural analysis confirmed that the prepared core-shell nanoparticles possess a cubic crystal structure with an average crystallite size of 52 nm. FESEM and HRTEM studies revealed that the Fe_3O_4:Gd@$NaYF_4$ product consists of spherical core-shell nanoparticles. The elemental distribution of Gd, Na, Y, and F within the samples was confirmed by EDS mapping. XPS analysis identified the valence states of the constituent elements in the prepared sample. Optical studies determined indirect bandgap values of 3.6 eV for Fe_3O_4:Gd and 3.25 eV for the Fe_3O_4:Gd@$NaYF_4$ core-shell nanoparticles, respectively. Cyclic voltammetry (CV) curves exhibited pseudocapacitive behavior, and the Fe_3O_4:Gd@$NaYF_4$ electrode showed a high specific capacitance of 612 F/g at a current density of 1 A/g. These results indicate that Fe_3O_4:Gd@$NaYF_4$ core-shell nanoparticles offer a promising platform for high-performance supercapacitor electrodes, owing to their synergistic combination of pseudocapacitance, conductivity, and structural stability, making them suitable for advanced energy storage systems.

Keywords: FESEM, VSM, Optical, Photocatalytic and Electrochemical properties**.**

1. Introduction

Global attention has been directed towards the investigation of renewable and sustainable energy-storage systems, such as Li-ion batteries, electrochemical hydrogen storage, and supercapacitors, in response to the rapid depletion of fossil fuels and environmental issues. In particular, supercapacitors have been identified as highly prospective applications for energy storage due to their rapid charge/discharge rate, high power density, low cost, and extended cycling life [1-4]. However, supercapacitors broad practical applications have been significantly impeded by their relatively low energy density. The efficiency of supercapacitors is predominantly determined by the electrode materials. Therefore, it is highly desirable to investigate high-energy-density electrode materials for supercapacitors in order to satisfy the needs of high-energy-density devices [5-8]. Based on the energy storage mechanism, supercapacitors can be categorized into two types: electrochemical double-layer capacitors (EDLCs), which rely on charge accumulation at the electrode/electrolyte interface, and pseudocapacitors, which arise from rapid redox processes occurring at electrochemically active sites [9]. Pseudocapacitors typically exhibit capacitance values that are at least 10 times greater than those of EDLCs when comparing the same specific surface area. Classic electrode materials for pseudocapacitance include metal oxides and conducting polymers [10].

Transition metal oxides such as Co_3O_4 [11], $NiCo_2O_4$ [12], Fe_3O_4 [13], $Ni(OH)_2$ [14], MnO_2 [15], etc. are compelling as pseudocapacitance electrode materials due to the multivalent states of their metallic ions and their crystal shapes, which facilitate rapid faradaic redox processes. Among metal oxides, magnetite (Fe_3O_4) is a notable option due to its environmental sustainability, natural abundance, cost-effectiveness, and diverse oxidation states [16]. The low electrical conductivity of iron oxide is a significant impediment to its application as an electrode material in electrochemical capacitors. To address this issue, three solutions have been developed: the fabrication of innovative nano-structures, metal ion doping, and composite based nanomaterials [17-18]. The introduction of core-shell structure is a promising approach to enhance the specific capacitance of electrode materials. Despite the numerous endeavours to improve electrochemical performance, the limited electron and ion transport remain the most pressing concerns for Fe_3O_4. The novel Fe_3O_4core-shell design is advantageous for the development of high-performance supercapacitors.

The Fe_3O_4:Gd@$NaYF_4$core-shell nanoparticles is an emerging multifunctional material that offers unique advantages for supercapacitor electrodes due to the synergistic integration of magnetic metal oxide (Fe_3O_4), rare-earth dopants (Gd^{3+}), and a luminescent host matrix ($NaYF_4$). Also, Fe_3O_4, commonly known as magnetite, is a well-known magnetic material with superparamagnetic properties that are invaluable in a range of applications including magnetic resonance imaging (MRI) and drug delivery systems [19, 20]. The introduction of gadolinium into the Fe_3O_4 configuration enhances the specific capacitance and material's magnetic resonance capabilities due to its high magnetic moment and excellent MRI contrast properties [21, 22].On the optical side, $NaYF_4$ is renowned for its upconversion luminescence, which is of considerable interest for various optical applications including bioimaging and photonic devices [23, 24]. To enhances the conductivity of Fe_3O_4:Gd and the cycling stability of $NaYF_4$, a combination of Fe_3O_4 and $NaYF_4$ can be utilized to form Fe_3O_4:Gd@$NaYF_4$ core-shell nanoparticles. Almost no literature exists that examines the applications of this material in supercapacitors. In these core-shell structures, the inorganic component serves as a strain buffer to ensure mechanical stability, while the $NaYF_4$ component functions as a conductor substance to improve the movement of electrons. In this context, the synthesis and characterization of Fe_3O_4:Gd@$NaYF_4$core-shell nanoparticles are of significant scientific and practical interest. Advances in synthesis techniques and characterization methods enable researchers to fine-tune the core-shell structure and better understand its properties, leading to improved electrochemical performance and broader application possibilities [25, 26]. Furthermore, the study of these materials under different electrical field conditions can reveal new aspects of their behavior and enhance their applicability in diverse fields such as electromagnetic devices and bioimaging systems [27, 28].

In this paper, a facile and hydrothermal method was employed to synthesize a Fe_3O_4:Gd@$NaYF_4$ core-shell nanoparticles, which was subsequently modified as the electrode for supercapacitors. The structural, morphology, optical and electrochemical properties of the Fe_3O_4:Gd@$NaYF_4$core-shell nanoparticleswere examined. Therefore, the core-shell electrode is distinguished by its exceptional cycling capability and prospective specific capacitance in comparison to Fe_3O_4:Gd. The Fe_3O_4:Gd@$NaYF_4$ core-shell nanoparticles are unquestionably a viable option for a supercapacitor electrode.

2. Experimental Procedure

2.1 Materials

Iron (II) sulphate heptahydrate ($FeSO_4.7H_2O$), Sodium sulphide flakes ($Na_2S.xH_2O$), Gadolinium (III) nitrate ($Gd(NO_3)_3$, Ammonium iron (III) sulfate dodecahydrate ($NH_4Fe(SO_4)_2.12H_2O$), Ferrous sulphate, Ferric sulphate, Ammonium solution, Sodium sulphide (Na_2s), Sodium fluoride (NaF), Poly vinyl pyrrolidone (PVP) were purchased from sigma company puducherry and were high-purity grade. All chemicals were used without further purification.

2.2.Synthesis of Fe_3O_4: Gd nanoparticles

Fe_3O_4 nanoparticles was first synthesized as the preparation of Ferric chloride hexahydrate ($FeCl_3.6(H_2O)$, 5mmol) and Ferrous chloride tetrahydrate ($FeCl_2.4(H_2O)$, 2mmol) were dissolved in deionized water at 100 ml and added Sodium sulphide flakes (3.6 g) and polymer (1.0 g) was added to the solution. Secondly gadolinium oxide was added in 50 ml of deionized water. The two homogeneous solutions were mixed together. The mixture was stirred energetically at 50°C for 30 minutes, and then transferred to a 100 mL Teflon-lined stainless-steel autoclave and maintained the temperature at 180°C for 6 hours. Afterthe completion of the reaction period, the autoclave was then allowed to cool to room temperature. The resulting black products was rinsed repeatedly with ethanol and then dried at 60°C for 6 hours.

2.3. Synthesis of $NaYF_4$ nanoparticles

The $NaYF_4$ nanoparticles were prepared by a facile hydrothermal method. To tailor their morphology and crystalline phase, the particles were obtained from the hydrothermal step using PVP as a surfactant. Firstly, 0.03M of Yttrium III acetate tetrahydrate and 0.02g of PVP were separately dissolved in 25 ml of deionized water and the stock solution was added dropwise to become a homogenous solution using a stirrer. Then, 50 ml of NaF solution (0.2 mol/L) was added dropwise to this mixture. After one hour of stirring for one h, the obtained particle suspension was centrifuged at 3000 rpm, washed once with ethanol and twice deionized water using centrifugation/ resuspension cycles and dried at 200°C using Teflon–line autoclave for 24h. After cooling, the mixture was centrifuged, separated, washed, and dried at 80°C for six h in an oven.

2.4. Synthesis of Fe_3O_4:Gd/$NaYF_4$ (Core/Shell NPs)

In a typical synthesis, 2.82 g of UCPs were dispersed in a solution containing ethanol (60 mL) and deionized water (40 mL) by sonication for 45 mins. Then 0.02g PVP was added to it. The mixture was again subjected to sonication for 1 h. Typically, 1.15g of dried Fe_3O_4 NPs was dissolved in 100 mL aqueous solution and then 3 mL of ammonia solution was added dropwise to it. The mixture was again subjected to sonication for one hour. Subsequently, UCPs solution was added dropwise to the above iron mixture solution under vigorous stirring. After stirring at room temperature for two hrs, the Fe_3O_4:Gd/$NaYF_4$ NPs were separated and washed repeatedly with deionized water to remove nonmagnetic by-products. Then the samples were dried in an oven (85°C) for 12 h. Finally, the resultant Fe_3O_4:Gd/$NaYF_4$ nanoparticles were used for further characterization

2.5. Materials Characterizations

Thermal analysis was performed using a NETZSCH-STA 449 F3 JUPITER instrument. Powder X-ray diffraction (XRD) patterns were collected on an XPertPro PW3050/60 X-ray diffractometer with Cu Kα radiation ($\lambda = 0.15406$ nm). Fourier-transform infrared (FTIR) spectroscopy was conducted on a Thermo Nicolet iS5 spectrometer to analyze the vibrational bands. The morphological characteristics were examined by field emission scanning electron microscopy (FESEM) using a CARL ZEISS-SIGMA 300 instrument. Energy-dispersive X-ray (EDX) spectroscopy and elemental mapping were performed concurrently with the FESEM studies. The size and shape of the nanoparticles were characterized using a FEI Technai G2 20 S-TWIN transmission electron microscope (TEM) operating at various resolutions. Samples for TEM were prepared by depositing a drop of dilute ethanol dispersion onto a copper grid and allowing it to dry. X-ray photoelectron spectroscopy (XPS) was carried out on an ULVAK-PHI

5000 VersaProbe III instrument with Al Kα radiation (hν = 1486.6 eV). Optical properties were investigated using a JASCO V-670 spectrophotometer. The electrochemical performance of the Fe_3O_4:Gd@$NaYF_4$ electrode was evaluated in a 3M KOH aqueous electrolyte at room temperature using an Autolab potentiostat.

3. Results and discussion

3.1. TG-DTA analysis

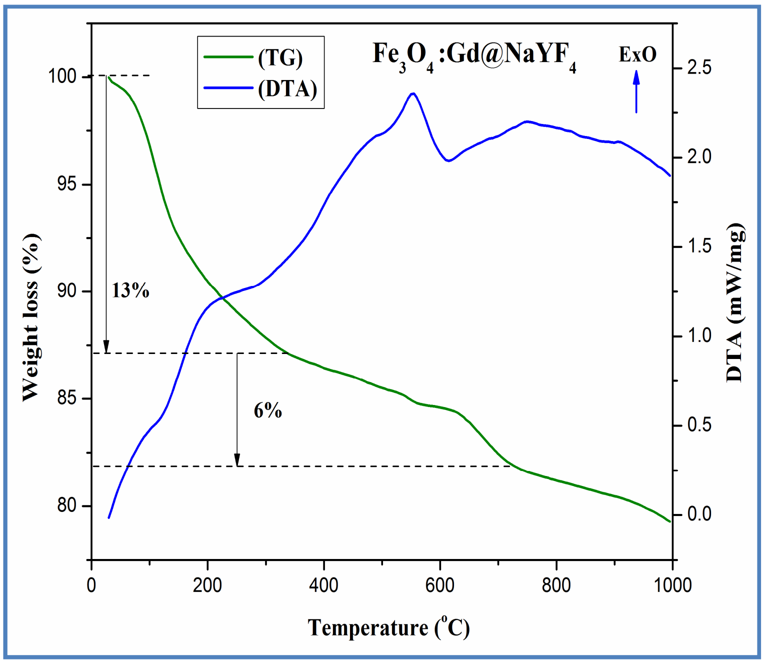

Fig. 1. TG-DTA analysis of as-prepared Fe_3O_4:Gd@$NaYF_4$ sample.

The thermal properties of the as-prepared sample were examined using simultaneous TG-DTA analysis, and the result is illustrated in Fig. 1. The TGA curve indicates a two-stage decomposition process occurring between room temperature and 1000 °C. An initial weight loss of 13% was observed between 20 °C and 360 °C, which is attributed to the evaporation of adsorbed water molecules. A further significant mass loss of 6% occurred between 361 °C and 710 °C, resulting from the complete combustion of carbon templates and organic residues. No significant weight loss was observed above 720 °C, and the absence of any exothermic peak in this region indicates the completion of the precursor's oxidation process. The endothermic peaks at approximately 180 °C and 550 ºC correspond to the decomposition of hydroxide species and a phase transition of the product, respectively.

3.2. XRD analysis

X-ray diffraction (XRD) was employed to analyze the crystal structures of Fe_3O_4:Gd and Fe_3O_4:Gd@$NaYF_4$ core-shell nanoparticles. Figure 1(a) shows the XRD pattern of the Fe_3O_4:Gd nanoparticles, where the observed diffraction peaks at 2θ angles of 30.72°, 35.44°, 43.05°, 53.93°, and 62.34° correspond to the (220), (311), (400), (422), and (440) crystal planes, respectively. The obtained diffraction peaks are consistent with a cubic crystal structure and match well with the standard JCPDS card no. 89-3854 [29]. Figure 1(b) shows the XRD pattern of the Fe_3O_4:Gd@$NaYF_4$ core-shell nanoparticles. Diffraction peaks associated with both Fe_3O_4:Gd and $NaYF_4$ are present, confirming the successful formation of the core-shell structure. The coating with $NaYF_4$ influenced the host lattice, leading to a progressive sharpening of the XRD peaks, which indicates enhanced crystallinity. The sharp, high-intensity diffraction peaks suggest that the Fe_3O_4:Gd@$NaYF_4$ core-shell nanoparticles are well-crystalline nature.

The crystallite size was calculated using the Debye-Scherrer formula, expressed as follows [30]:

$$D = (0.89\lambda) / (\beta \cos\theta) \tag{1}$$

where λ is the X-ray wavelength, β is the full width at half maximum (FWHM), D is the crystallite size, and θ is the Bragg angle. The calculated crystallite sizes were found to be 58 nm and 62 nm for the Fe_3O_4:Gd and Fe_3O_4:Gd@$NaYF_4$ core-shell nanoparticles, respectively. The increase in crystallite size for the core-shell structure is consistent with the observed sharpening of the diffraction peaks. These changes suggest improved crystallite growth and enhanced longrange order within the crystal structure. The enhanced crystallinity typically results in better charge transport pathways and reduced internal resistance, which are critical for high-rate electrochemical performance. Furthermore, moderate crystallite growth can increase the number of active sites for redox reactions without severely compromising the surface area. This structural evolution correlates well with the observed enhancement in specific capacitance.

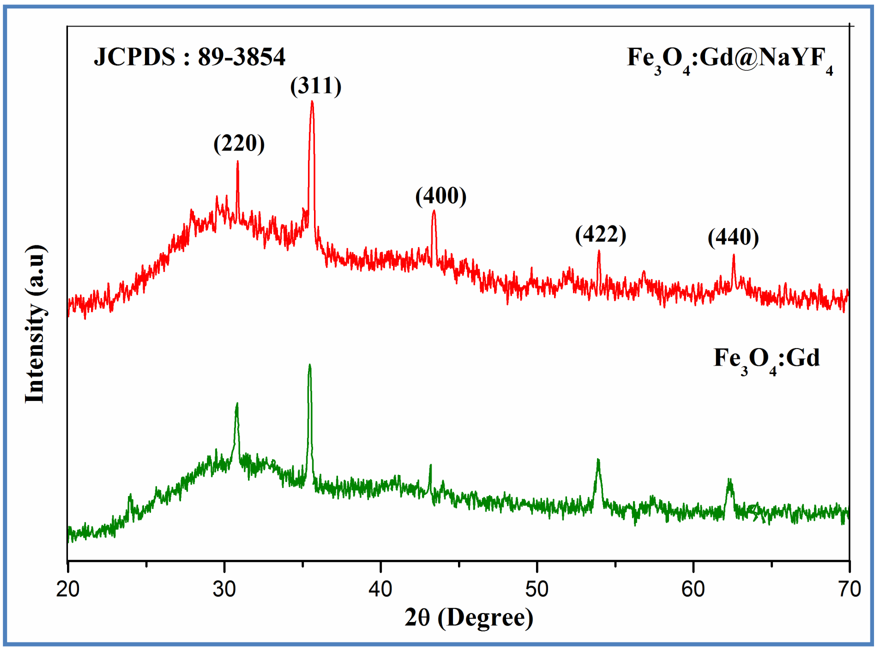

Fig. 2. XRD patterns of Fe_3O_4:Gd@$NaYF_4$ core-shell nanoparticles.

3.3. FTIR analysis

The characteristic interatomic bands formed between the constituent elements of the material were investigated by analyzing its infrared spectrum, as illustrated in Fig. 3. The introduction of rare-earth ions into ferrites results in various physical and structural modifications. These structural changes, induced by metal ions, significantly influence lattice vibrations. Furthermore, factors such as cation mass, cation-oxygen bonding, and bonding force affect these vibrations, which vary with dopant concentration. As shown in Fig. 3, strong vibration bands were detected at 593, 1082, 1371, 1604, and 3454 cm^{-1}. The broad bands at 3454 and 1604 cm^{-1} were attributed to the O-H stretching and H-O-H bending vibrations of adsorbed water molecules, respectively [31, 32]. The absorption bands at 1082 and 1371 cm^{-1} are consistent with the C-O and C=O stretching vibrations, respectively [33]. The band observed at 593 cm^{-1} is indicative of metal-oxygen bonds. Two primary absorption bands were identified at approximately 443 cm^{-1} and 586 cm^{-1}, which are attributable to the stretching vibrations of metal-oxygen bonds (Gd/Fe–O) at tetrahedral and octahedral sites, respectively [34].

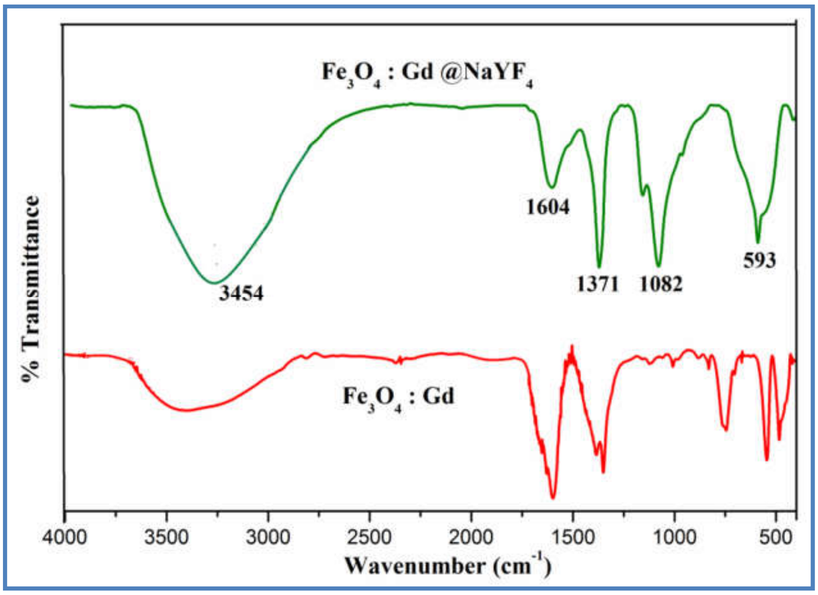

Fig. 3. FTIR spectrum of Fe_3O_4:Gd@$NaYF_4$ core-shell nanoparticles.

3.4. FESEM analysis

The morphology of the synthesized products was examined using FESEM and the results, depicted in Fig. 4(a,b), indicate that the Fe_3O_4:Gd nanoparticles are relatively monodisperse and possess a spherical morphology. Figure 4(d,e) presents FESEM images of the Fe_3O_4:Gd@$NaYF_4$ core-shell nanoparticles. This analysis reveals a significant alteration in both particle size and morphology, which is attributable to the deposition of a $NaYF_4$ shell onto the Fe_3O_4:Gd core nanoparticles. The Fe_3O_4:Gd@$NaYF_4$ core-shell nanoparticles show that the spherical particles are attached to each other, forming cluster-like structures. The spherical morphology and larger specific surface area of the Fe_3O_4:Gd@$NaYF_4$ core-shell structure facilitate ion diffusion and improve capacitive performance. The average grain size was determined from these micrographs using Image J software. Histogram analysis, illustrated in Fig. 4(c,f), reveals average grain sizes of 62 nm and 75 nm for the Fe_3O_4:Gd and Fe_3O_4:Gd@$NaYF_4$ core-shell nanoparticles, respectively. The average grain size values are larger than the crystallite sizes obtained from XRD analysis. This indicates that each grain observed by FESEM is polycrystalline and consists of multiple smaller crystallites, thereby corroborating the XRD findings.

3.5. EDS mapping analysis

Energy-dispersive X-ray spectroscopy (EDS) mapping was utilized to determine the elemental composition and distribution of both samples, as illustrated in Fig. 5(a–f). The elemental maps clearly show the spatial distribution of all detected elements within the prepared samples. The uniform distribution of the signals for Fe, Gd, O, Na, Y, and F in the EDS mapping confirms the presence of these elements. The spectra demonstrate the absence of any significant impurities, confirming the successful synthesis of the Fe_3O_4:Gd@$NaYF_4$ core-shell nanoparticles.

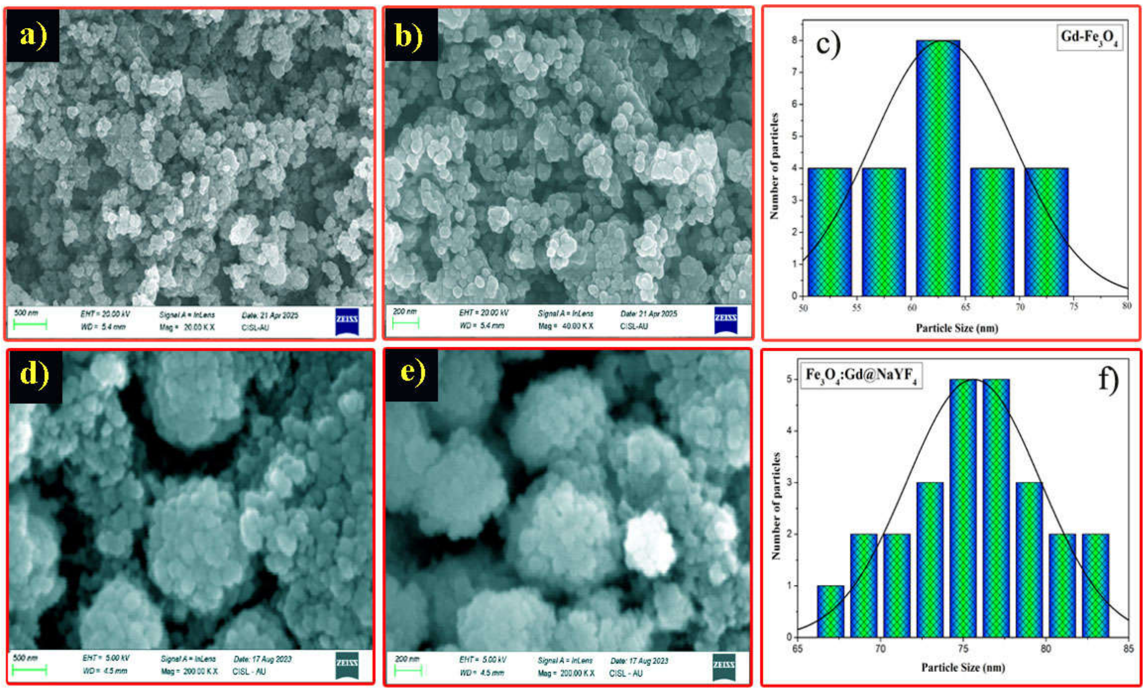

Fig. 4. FESEM images (a,b) Fe_3O_4:Gd, (d,e) Fe_3O_4:Gd@$NaYF_4$core-shell nanoparticles and corresponding histogram images (c, f).

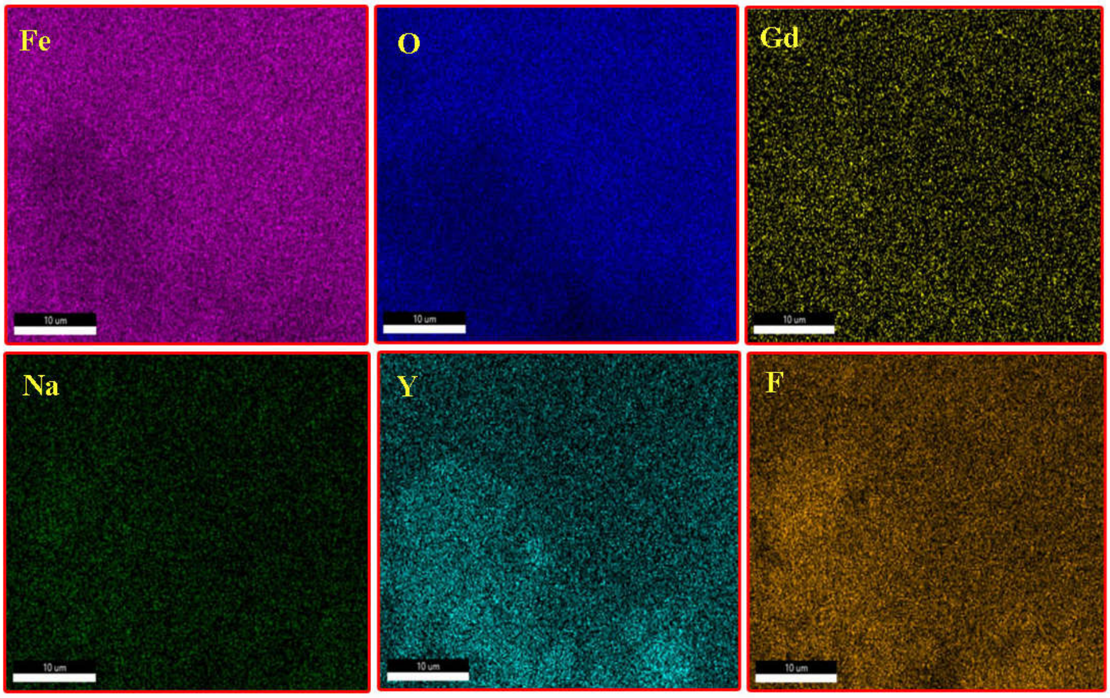

Fig. 5.EDS mapping images of Fe_3O_4:Gd@$NaYF_4$ core-shell nanoparticles.

3.6. HRTEM analysis

High-Resolution Transmission Electron Microscopy (HRTEM) was utilized to examine the morphology and structure of the Fe_3O_4:Gd and Fe_3O_4:Gd@$NaYF_4$ core-shell nanoparticles. The HRTEM micrographs, shown in Figs. 6(a,b) and Figs. 6(e,f), reveal spherical particles for the Fe_3O_4:Gd sample and cluster-type formations for the Fe_3O_4:Gd@$NaYF_4$ core-shell nanoparticles. This core-shell architecture is anticipated to deliver exceptional supercapacitor performance due to synergistic interactions between its constituent materials. The lattice fringes of both samples are presented in Figs. 6(c) and Figs. 6(g). The measured interplanar spacing of 0.25 nm and 0.34 nm correspond to the (311) plane of Fe_3O_4:Gd and the (111) plane of the $NaYF_4$ shell, respectively, confirming the successful formation of the heterostructure. The selected area electron diffraction (SAED) patterns, shown in Figs. 6(d) and Figs. 6(h), display distinct diffraction spots, indicating the polycrystalline nature of both samples. These findings are consistent with the results obtained from FESEM analysis.

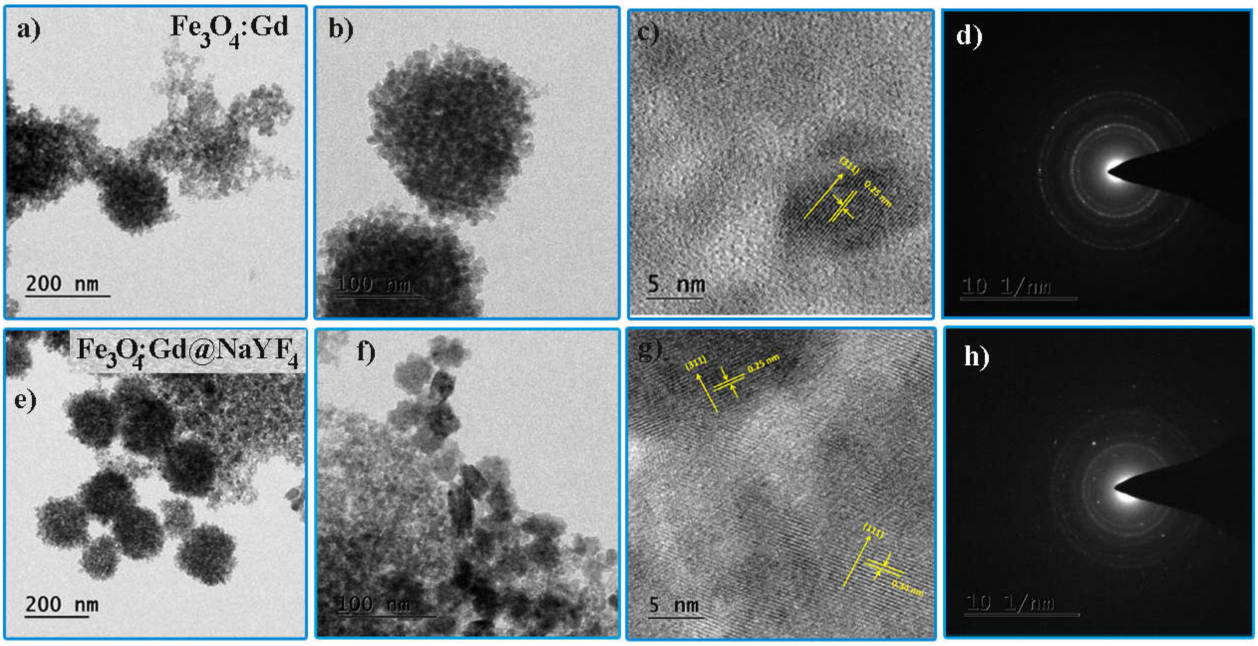

Fig. 6.HRTEM analysis of Fe_3O_4 : Gd nanoparticles (a,b) images(c) lattice spacing, (d) SAED pattern, and Fe_3O_4:Gd@$NaYF_4$core-shell nanoparticles (a,b) images(c) lattice spacing, (d) SAED pattern

3.7. XPS analysis

X-ray photoelectron spectroscopy (XPS) was employed to ascertain the presence of constituent elements, their chemical states, and the successful formation of the Fe_3O_4:Gd@$NaYF_4$ core-shell structure. The XPS spectra of the core-shell nanoparticles were investigated to understand their electronic interactions, with the results illustrated in Fig. 7. The survey scan spectrum in Fig. 7(a) confirms the presence of *Fe 2p, Gd 4d, Na 1s, Y 3p, F 1s*, and *O 1s*, thereby verifying the existence of all expected elements in the core-shell nanoparticles. Figure 7(b) displays the high-resolution Fe 2p spectrum, with two major characteristic peaks for Fe $2p_{3/2}$ and Fe $2p_{1/2}$ located at binding energies of 711.6 eV and 725.5 eV, respectively [35]. The spin-energy separation of approximately 14.1 eV between the Fe 2p peaks is characteristic of Fe^{2+} ions. The Gd 4d spectrum (Fig. 7(c)) shows two major peaks at binding energies of 141.8 eV and 147.6 eV, corresponding to Gd $4d_{5/2}$ and Gd $4d_{3/2}$, respectively. The separation of approximately 6.1 eV between these peaks is in agreement with the reported values for Gd^{3+} ions [36]. The O 1s spectrum (Fig. 7(d)) can be deconvoluted into two components. The peak located at 531.5 eV is attributed to adsorbed oxygen species (O_ads) in oxygen-deficient regions. The presence of adsorbed oxygen species enhances capacitive performance by contributing to pseudocapacitance and improving electrode-electrolyte wettability [37]. The Na 1s spectrum (Fig. 7(e)) exhibits a peak at 1074 eV, confirming the Na^+ oxidation state [38]. Figure 7(f) presents the high-resolution Y 3p spectrum, with peaks at 308.5 eV and 320.2 eV corresponding to Y $3p_{3/2}$ and Y $3p_{1/2}$, respectively, indicating the Y^{3+} state. Finally, the F 1s spectrum (Fig. 7(g)) shows a single peak at 688.4 eV, confirming the presence of fluorine in its -1 oxidation state [39].

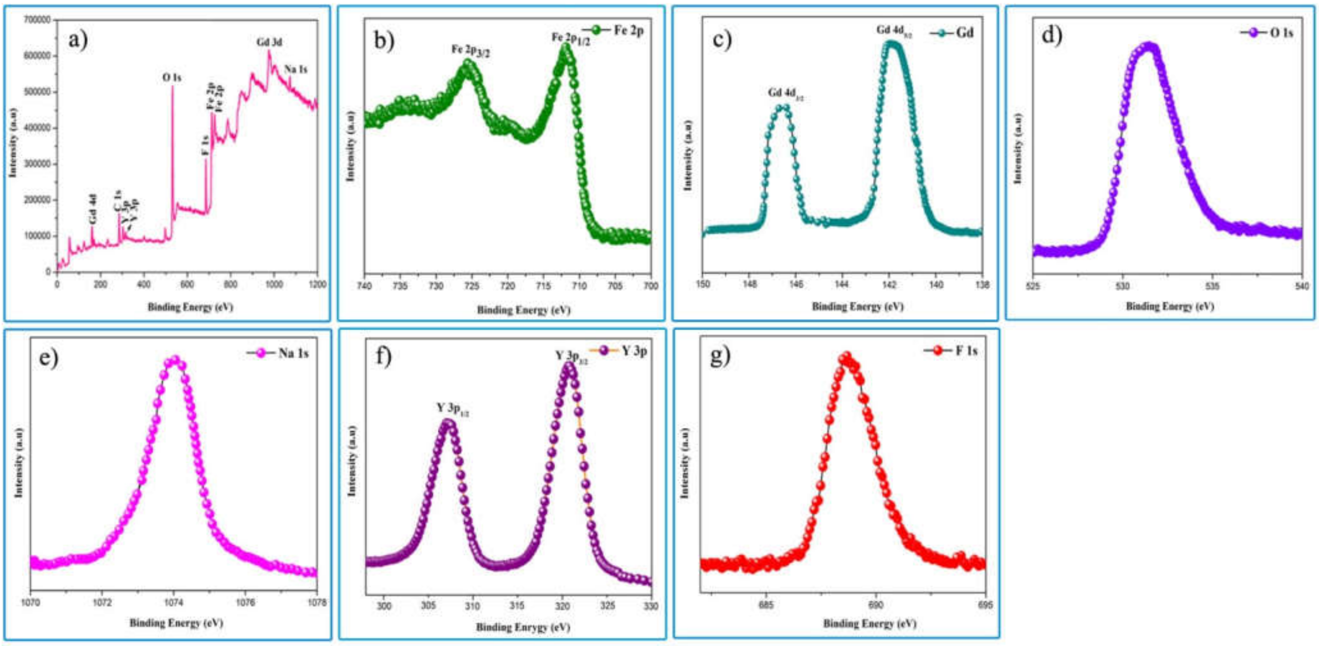

Fig. 7. XPS spectrum of Fe_3O_4:Gd@$NaYF_4$ core-shell nanoparticles (a) survey scan, (b) Fe 2P, (c) Gd 3d, (d) O 1s, (e) Na 1s, (f) Y 3p, (g) F 1s

3.8. Optical Properties

The optical properties of Fe_3O_4:Gd and Fe_3O_4:Gd@$NaYF_4$ core-shell nanoparticles were investigated using UV-Vis spectroscopy, and the resulting spectra are presented in Fig. 8(a). The Fe_3O_4:Gd@$NaYF_4$ core-shell nanoparticles exhibit enhanced absorption across the visible spectrum. Figure 8 clearly shows that the light absorption characteristics are augmented over the entire visible range. This alteration in the electronic structure of the core-shell nanoparticles may enhance electrochemical performance by facilitating faster ion transport within the $NaYF_4$ shell and expediting ion delivery to reaction sites.

The energy band gap can be difficult to estimate directly from absorption spectra; consequently, it is determined by Tauc's plots using Eq. (2)[40].

$$\alpha h\nu = A(h\nu - Eg)^n \quad (2)$$

where ‘h ’ is excitation energy, ‘Eg’ is the optical band gap, ‘P’ is theproportionality parameter that depends on electron transitionprobability, and ‘n’ is the index number that signifies the nature ofthe energy band transition. The direct permitted transition is quantified by selecting the appropriate exponent value, specifically n = 1/2. Figure. 8(b) represents the optical bandgap of Fe_3O_4:Gd and Fe_3O_4:Gd@$NaYF_4$ core-shell nanoparticles, and plots the linear part of $(\alpha h\nu)^2$ on the y-axis versus hνon the x-axis. The calculated bandgap values were 3.6 eV and 3.25 eV for Fe_3O_4:Gd and Fe_3O_4:Gd@$NaYF_4$ core-shell nanoparticles, respectively. The observed decrease in the bandgap with increasing crystallite size can be attributed to the quantum confinement effect. In larger crystallites, a finite number of atoms are tightly bonded (including Coulombic forces), leading to a greater overlap of atomic orbitals compared to smaller crystallites. This enhanced orbital overlap generates new energy states within the bandgap, thereby reducing its width. Consequently, the observed reduction in bandgap is consistent with the increase in crystallite size resulting from the incorporation of the $NaYF_4$ shell[41].

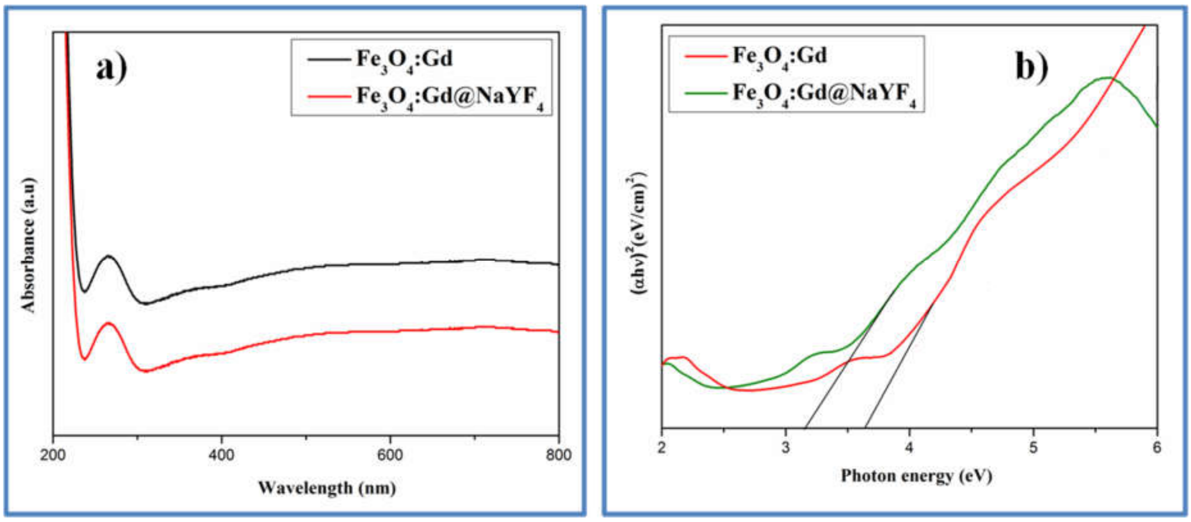

Fig. 8. Optical properties of Fe_3O_4:Gd@$NaYF_4$ core-shell nanoparticles
(a) UV-Vis, (b) Bandgap.

3.9. Magnetic analysis

The magnetic characteristics of the prepared core-shell nanoparticles were investigated using a vibrating sample magnetometer (VSM) at room temperature. It was observed that both samples exhibited a strong magnetic response to an applied magnetic field. The magnetization (M, emu/g) as a function of the applied magnetic field (H, Oe) over a range of -15,000 to 15,000 Oe is depicted in Fig. 9. The hysteresis loops indicate that both samples exhibit ferromagnetic behavior. The saturation magnetization (Ms) values for the Fe_3O_4:Gd and Fe_3O_4:Gd@$NaYF_4$ core-shell nanoparticles were 51.08 emu/g and 32.65 emu/g, respectively. The reduction in saturation magnetization for the core-shell structure is attributed to the presence of the non-magnetic $NaYF_4$ shell coating the magnetic Fe_3O_4 core. This coating reduces the magnetic moment at the core-shell interface due to interactions between magnetite and the $NaYF_4$ shell, as well as a diamagnetic shielding effect proportional to the volume ratio of the shell to the entire nanoparticle. The coercivity (Hc), which is the reverse field strength required to reduce the magnetization to zero, decreased from 3.68 Oe for Fe_3O_4:Gd to 2.25 Oe for the Fe_3O_4:Gd@$NaYF_4$ core-shell nanoparticles. This reduction can be attributed to decreased interparticle interactions and changes in magnetoelastic anisotropy. The formation of the $NaYF_4$ shell around the magnetic core induces surface stress, which increases the magnetoelastic anisotropy. The low coercivity and remanence values suggest the core-shell nanoparticles exhibit near-superparamagnetic behavior at room temperature. The remanence (Mr), which is the magnetization remaining at zero field, was 5.16 emu/g for Fe_3O_4:Gd and 3.69 emu/g for the Fe_3O_4:Gd@$NaYF_4$ core-shell nanoparticles. This study demonstrates that coating with $NaYF_4$ modifies the magnetic properties of Fe_3O_4:Gd. The resulting near-superparamagnetic characteristics of the Fe_3O_4:Gd@$NaYF_4$ core-shell nanoparticles suggest their potential suitability for biomedical and supercapacitor applications.

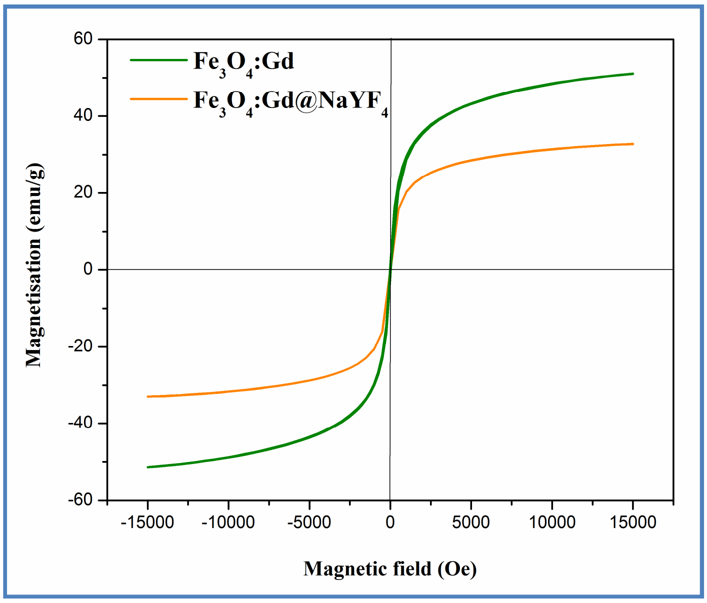

Fig. 9. VSM analysis of Fe_3O_4:Gd@$NaYF_4$ core-shell nanoparticles**.**

3.10. Electrochemical analysis

3.10.1. Cyclic Voltammetry

To assess the potential applications in electrochemical capacitors, electrodes were fabricated from Fe_3O_4:Gd and Fe_3O_4:Gd@$NaYF_4$ core-shell nanoparticles and tested in a three-electrode configuration, as illustrated in Fig. 10. The cyclic voltammetry (CV) profiles of the Fe_3O_4:Gd@$NaYF_4$ electrode in a 3M KOH aqueous electrolyte at varying scan rates are depicted in Fig. 10. The prepared electrodes exhibited oxidation/reduction peaks, confirming pseudocapacitor behavior. Furthermore, as the scan rate increases, the largely rectangular shapes accompanied by broad oxidation/reduction humps persist, suggesting that the electrode exhibits significant reversibility and excellent rate capability. The specific capacitance was assessed using cyclic voltammetry curves [42].

$$C_s = \frac{\int I\,dv}{m \times s \times V} \qquad (3)$$

Where I.dv is the charge obtained from the CV curves, 'm' is the mass of the active material in the electrode (mg), 'v' is potential window and 's' is the scan rate (mV/s). According to the CV curves, Fe_3O_4:Gd electrode exhibited the capacitance values of 520, 485, 432, 393, 330, 272, and 230 F/g at scan rates of 5, 10, 15, 25, 50, 75, and 100 mV/s, respectively. Likewise, the Fe_3O_4:Gd@$NaYF_4$electrode had maximum capacitance values of 565, 531, 460, 366, 264, 248, and 216 Fg^{-1} at 5, 10, 15, 25, 50, 75, and 100 mV/s, respectively. The enhanced capacitive performance of the Fe_3O_4:Gd@$NaYF_4$ core-shell nanoparticles is attributed to their highly porous cluster architecture. This structure facilitates more efficient ion and electron transport throughout the porous matrix. At lower scan rates, electrolyte ions have sufficient time to fully intercalate and deintercalate into the active material. This process optimizes the utilization of the electrode material, thereby achieving a higher specific capacitance [43].

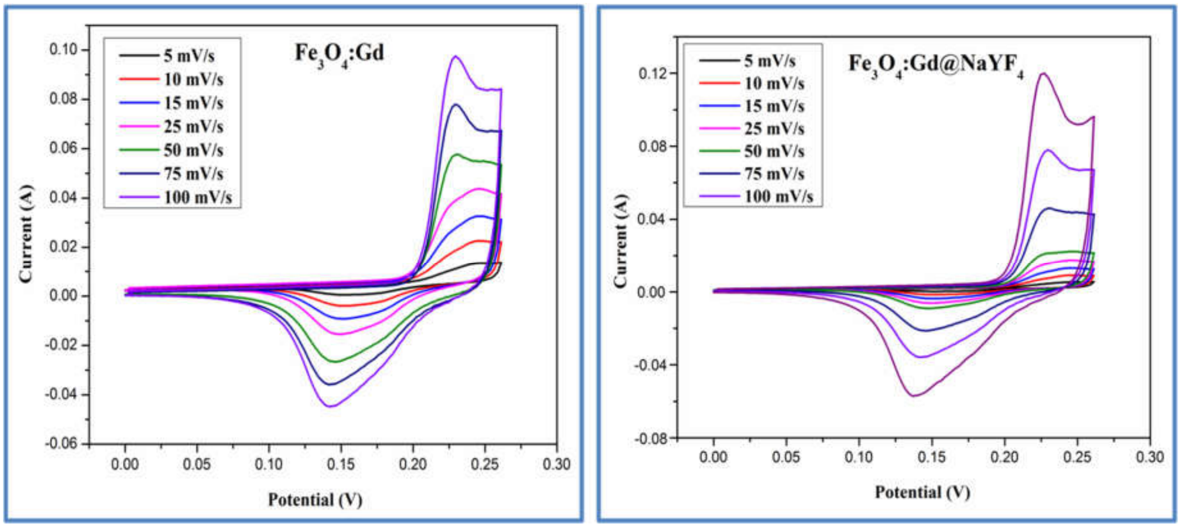

Fig. 9. Cyclic voltammetry spectrum of Fe_3O_4:Gd@$NaYF_4$ core-shell nanoparticles.

3.9.2. Galvanostatic charge discharge analysis

The galvanostatic charge-discharge (GCD) curves of the Fe_3O_4:Gd and Fe_3O_4:Gd@$NaYF_4$ core-shell electrodes, prepared with varying molar ratios and tested at different current densities are shown in Fig. 11. The potential window was 0–0.25 V. The nonlinear discharge curves and the presence of voltage plateaus further confirm the pseudocapacitive behavior of both electrodes, as they correspond well with the redox peaks observed in the CV curves. The specific capacitance values (Cs) were calculated from the discharge curves using the standard formula [44]. The Fe_3O_4:Gd electrode exhibited specific capacitances of 580, 460, 324, 288, and 231 Fg^{-1} at current densities of 1, 2, 3, 4, and 5 Ag^{-1}, respectively. In comparison, the Fe_3O_4:Gd@$NaYF_4$ electrode showed a higher specific capacitances of 612, 563, 485, 352, and 240 Fg^{-1} at the same respective current densities. The GCD results demonstrate that the Fe_3O_4:Gd@$NaYF_4$ electrode possesses a superior specific capacitance compared to the Fe_3O_4:Gd electrode. This enhancement is attributed to the presence of the $NaYF_4$ shell, which provides a larger electroactive surface area and facilitates more efficient electron transport pathways. The synergistic interaction between the $NaYF_4$ shell and the Fe_3O_4:Gd core contributes to the substantial improvement in capacitive performance.

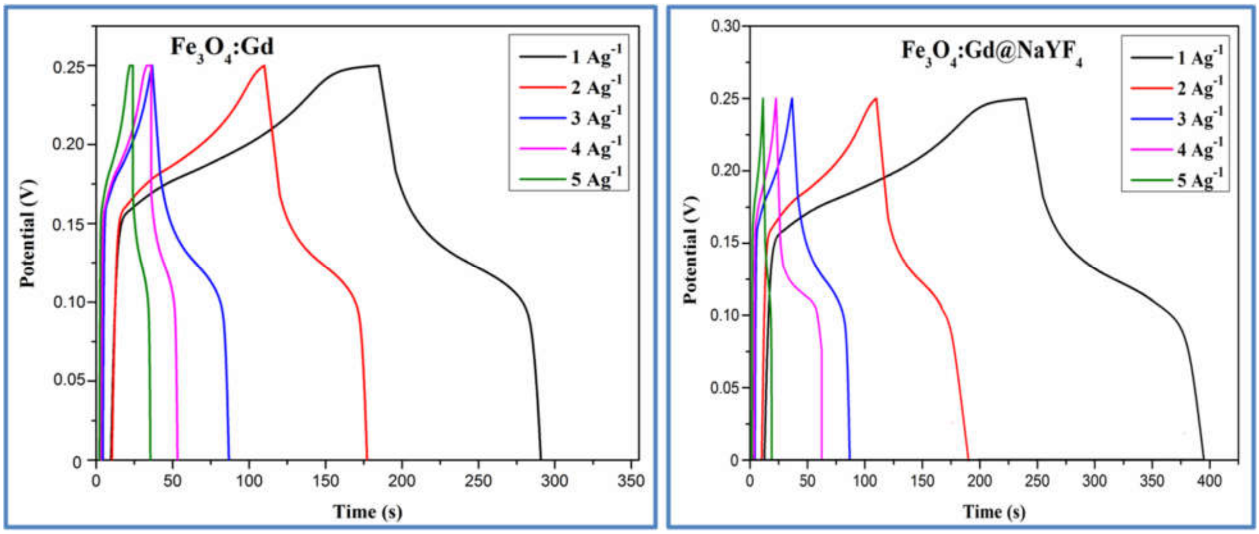

Fig. 11. Galvanostatic charge and discharge profile of Fe_3O_4:Gd@$NaYF_4$ core-shell nanoparticles.

3.9.3. Electrochemical impedance spectroscopy (EIS)

To examine the charge carrier transport characteristics of the Fe_3O_4:Gd and Fe_3O_4:Gd@$NaYF_4$ electrodes, electrochemical impedance spectroscopy (EIS) was performed. The EIS spectra presented in Fig. 12 show that both Nyquist plots consist of a semicircular arc in the high-frequency region and an inclined line in the low-frequency region. The internal resistance (Rs), observed from the high-frequency intercept on the real axis, includes the intrinsic resistance of the electrode active material, the bulk resistance of the electrolyte, and the contact resistance at the active material/current collector interface. The diameter of the semicircle corresponds to the charge transfer resistance (Rct). In the low-frequency region, the linear component represents the Warburg impedance (W), which is associated with ion diffusion resistance. A steeper slope indicates lower diffusion resistance and faster ion transport. Figure 12 shows that the slope of the line for the Fe_3O_4:Gd@$NaYF_4$ core-shell electrode is steeper than that of the Fe_3O_4:Gd electrode, indicating superior ion diffusion kinetics. Furthermore, the

Fe_3O_4:Gd@$NaYF_4$ core-shell electrode exhibits a smaller high-frequency intercept on the real axis compared to the Fe_3O_4:Gd electrode, indicating a lower internal resistance (Rs). This enhanced conductivity is attributed to the incorporation of a highly conductive $NaYF_4$ shell [45].

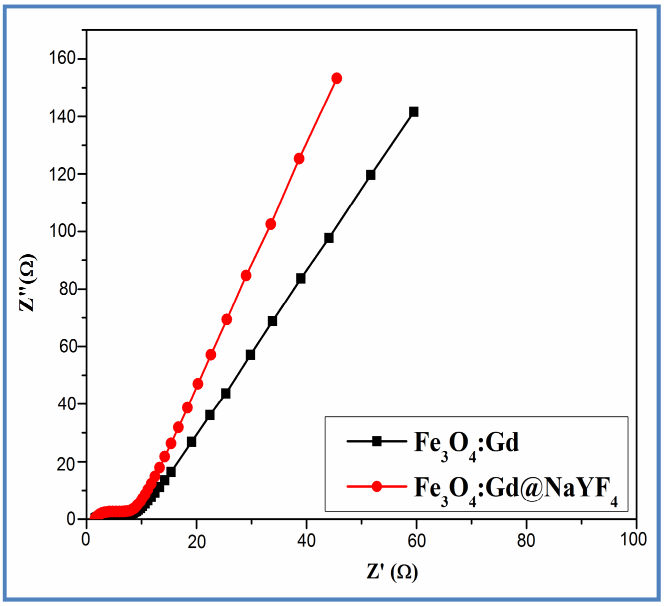

Fig. 12. EIS spectrum of Fe_3O_4:Gd@$NaYF_4$ core-shell nanoparticles.

3.10. Photocatalytic activity

The photocatalytic degradation of methylene blue (MB) dye using Fe_3O_4:Gd and core-shell Fe_3O_4:Gd@$NaYF_4$ nanoparticles under sunlight irradiation leverages the synergistic interplay of magnetic recyclability and enhanced visible-light absorption mechanisms (Fig. 13). The gadolinium-doped magnetite (Fe_3O_4:Gd) core facilitates efficient charge separation and reduces electron-hole recombination due to Gd^{3+} incorporation, which introduces oxygen vacancies and modifies the band structure to narrow the bandgap, thereby improving visible-light absorption [46]. Simultaneously, the magnetic properties enable effortless catalyst recovery using an external magnet, addressing reuse challenges in wastewater treatment. When coated with a $NaYF_4$ shell, the nanocomposite gains upconversion capabilities, converting near-infrared (NIR) photons from sunlight into higher-energy visible or ultraviolet light, which further excites the photocatalyst and broadens the solar spectrum utilization. This NIR-driven mechanism is critical for activating wide-bandgap semiconductors and generating reactive oxygen species (ROS) like ·OH and $\cdot O_2^-$, which drive MB degradation via oxidative cleavage of its chromophoric structure. The combination of Gd-induced electronic modulation, upconversion-mediated light harvesting, and magnetic separability positions these nanoparticles as sustainable photocatalysts for solar-driven environmental remediation.

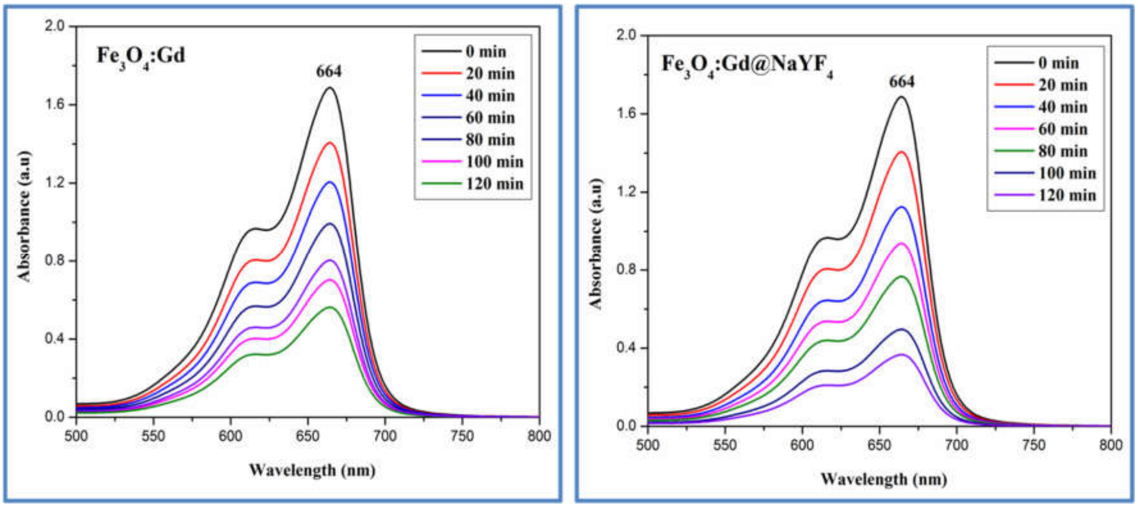

Fig. 13. UV-Visible absorbance of MB degradation using Fe_3O_4:Gd@$NaYF_4$ core-shell nanoparticles.

4. Conclusion

Fe_3O_4:Gd@$NaYF_4$ core-shell nanoparticles demonstrate significant potential for next-generation supercapacitor applications due to their unique structural, magnetic, and electrochemical properties. The Fe_3O_4:Gd@$NaYF_4$ core-shell nanoparticles were effectively prepared using a simple hydrothermal approach. The FESEM and HRTEM studies revealed the $NaYF_4$ nanoparticles were formed as a shell around spherical structure Fe_3O_4:Gd nanoparticles which forms the core. The XRD patterns show that the $NaYF_4$ does not alter the crystal structure of Fe_3O_4:Gd. The presence of metal oxide vibrational bands was confirmed by FTIR analysis.

XPS studies verified the oxidation state of core-shell nanoparticles of Na^+ and Y^{3+}. For photocatalytic activity, the spherical structure core-shell was studied as photocatalyst under illumination of sunlight, the MB dye degradation efficiency was about 80% after 120 mins. The magnetic Fe_3O_4 core, doped with Gd^{3+}, enhances electron mobility and conductivity, while the $NaYF_4$ shell provides surface stability, prevents agglomeration, and offers a platform for surface functionalization. This synergistic core-shell structure enables high specific capacitance (612 Fg^{-1}), and improved charge-discharge efficiency. Furthermore, the incorporation of rare-earth elements like Gd, Na and Y introduces tunable properties, which can be tailored for multifunctional energy storage systems.

References

1. L. Kong, X. Chen, B. Q. Li, H. J. Peng, J. Q. Huang, J. Xie, Q. Zhang, Adv. Mater. 2018, 30, 1705219
2. Z. M. Liu, T. C. Lu, T. Song, X. Y. Yu, X. W. Lou, Energy Environ. Sci.2017, 10, 1576.
3. Q. K. Hu, D. D. Sun, Q. H. Wu, H. Y. Wang, L. B. Wang, B. Z. Liu,A. G. Zhou, J. L. He, J. Phys. Chem. A 2013, 117, 14253.
4. K. Fu, O. Yildiz, H. Bhanushali, Y. X. Wang, K. Stano, L. G. Xue,X. W. Zhang, P. D. Bradford, Adv. Mater. 2013, 25, 5109
5. T. Wei, M. Zhang, P. Wu, Y. J. Tang, S. L. Li, F. C. Shen, X. L. Wang,X. P. Zhou, Y. Q. Lan, Nano Energy 2017, 34, 205.
6. L. F. Chen, Z. H. Huang, H. W. Liang, W. T. Yao, Z. Y. Yu, S. H. Yu,Energy Environ. Sci. 2013, 6, 3331.
7. M. Saraf, K. Natarajan, S. M. Mobin, ACS Appl. Mater. Interfaces 2018, 10, 16588.
8. L. F. Shen, L. Yu, H. B. Wu, X. Y. Yu, X. G. Zhang, X. W. Lou,Nat. Commun. 2015, 6, 6694
9. E. Pardieu, S. Pronkin, M. Dolci, T. Dintzer, B.P. Pichon, D. Begin, C. Pham-Huu, P. Schaaf, S. Begin-Colin, F. Boulmedais, Hybrid layer-by-layer composites based on a conducting polyelectrolyte and Fe_3O_4 nanostructures grafted onto

graphene for supercapacitor application, J. Mater. Chem. A 3 (2015) 22877-22885.

10. Yong Ma, Chunping Hou, Hepeng Zhang, Qiuyu Zhang, Hu Liu, Shide Wu, Zhanhu Gu, Three-dimensional core-shell Fe_3O_4/Polyaniline coaxial heterogeneous nanonets: Preparation and high performance supercapacitor electrodes, ElectrochimicaActa, 315, (2019), 114-123. https://doi.org/10.1016/j.electacta.2019.05.073
11. K. Ding, P. Yang, P. K. Hou, X. L. Song, T. Wei, Y. Q. Cao, X. Cheng,Adv. Mater. Interfaces 2017, 4, 1600884
12. C. Y. Cao, W. Guo, Z. M. Cui, W. G. Song, W. Cai, J. Mater. Chem.2011, 21, 3204
13. J. W. Zhou, C. Zhang, T. X. Niu, R. X. Huang, S. Li, J. Z. Zhang,J. G. Chen, A. C. S. Appl, Energy Mater. 2018, 1, 4599.
14. S. Anwer, A. B. Ari, G. Bharath, P. Cao, S. P. Patole, S. H. Luo,H. T. Masood, W. J. Cantwell, K. Liao, Q. W. Li, L. X. Zheng, Adv.Mater. Interfaces 2019, 6, 1900670
15. L. Mao, K. Zhang, H. S. O. Chan, J. S. Wu, J. Mater. Chem. 2012,22, 1845
16. Nithya VD, Arul NS. Progress and development of Fe3O4 electrodes for supercapacitors. *Journal of Materials ChemistryA*. 2016;4(28):10767-10778
17. Guo Z, Shin K, Karki AB, Young DP, Kaner RB, Hahn HT. Fabrication and characterization of iron oxide nanoparticlesfilled polypyrrole nanocomposites. *Journal of NanoparticleResearch*. 2009;11(6):1441-1452
18. Li L, Gao P, Gai S, He F, Chen Y, Zhang M, et al. Ultra-smalland highly dispersed Fe3O4 nanoparticles anchored on reducedgraphene for supercapacitor application. *ElectrochimicaActa*. 190, (2016) 566-573.
19. Yang X, Kan J, Zhang F, Zhu M, Li S. Facile Fabrication of Mn^{2+} Doped Magnetite Microspheres as Efficient Electrode Material for Supercapacitors. Journal of Inorganic and Organometallic Polymers and Materials. 2017;27(2):542-551
20. J. S. M. L. Goss, Magnetite nanoparticles for drug delivery and imaging applications, Journal of Nanoparticle Research, vol. 16, no. 4, pp. 213-223, 2014
21. S. S. K. R. D. A. K. Patel, Gadolinium-based contrast agents for MRI, Journal of Magnetic Resonance Imaging, vol. 42, no. 3, pp. 589-598, 2015

22. M. A. C. de Almeida, Gadolinium: Magnetic properties and biomedical applications, Physics Reports, vol. 543, pp. 1-23, 2014
23. X. Zhang, Y. Zhang, Upconversion luminescence in $NaYbF_4$ materials, Journal of Luminescence, vol. 158, pp. 128-135, 2015
24. H. Z. S. Liu, Rare earth upconversion nanoparticles for biological imaging, Chemical Society Reviews, vol. 43, no. 6, pp. 2373-2384, 2014
25. G. Y. H. Y. Zhang, Synthesis techniques for core-shell materials, Materials Science and Engineering: R: Reports, vol. 88, pp. 1-28, 2015
26. N. D. H. Q. Lu, Characterization methods for core-shell nanoparticles, Analytical Chemistry, vol. 86, no. 14, pp. 6871-6880, 2014
27. L. J. C. Liu, Impact of electric fields on core-shell material performance, Scientific Reports, vol. 7, no. 1, pp. 1289-1300, 2016
28. Y. X. W. Zhao, Characterization of core-shell materials under varying electric fields, Journal of Physical Chemistry C, vol. 120, no. 24, pp. 13877-13885, 2016
29. Hongtao Cui , WanzhongRen , Peng Lin & Yan Liu (2013) Structure controlsynthesis of iron oxide polymorph nanoparticles through an epoxide precipitation route, Journal ofExperimental Nanoscience, 8:7-8, 869-875
30. B. Guo, A. FinneWistrand, A.C. Albertsson, Degradable and electroactive hydrogels with tunable electrical conductivity and swelling behavior, Chem. Mater. (2011)
31. S. Xing, Z. Zhou, Z. Ma, Y. Wu, Characterization and reactivity of Fe3O4/FeMnOx core/shell nanoparticles form ethylene blue discoloration with H2O2, Appl. Catal. B Environ. 107 (2011) 386–392. DOI:10.1016/j.apcatb.2011.08.002
32. S. Kumari, E. Sharma, J. Verma, J. Dalal, A. Kumar, Structural and photoluminescence properties of Dy-doped nanocrystalline ZrO_2 for optoelectronics application, Ceram. Int. 49 (2023) 20185–20192. https://doi.org/10.1016/j.ceramint.2023.03.142
33. J.P. Singh, G. Dixit, R.C. Srivastava, H.M. Agrawal, K. Asokan, Looking for the possibility of multiferroism in $NiGd_{0.04}Fe_{1.96}O_4$ nanoparticle system, J. Phys. D Appl. Phys. 44 (2011) 435306

34. NeerajKadian, RenuKumari, AnkitPanchal, JasvirDalal, DiwakarPadalia, Structural and optical properties of gadolinium doped-magnetite nanocrystal for photocatalytic application, Journal of Alloys and Compounds 960 (2023) 170811.
35. H.G. Cha, M.J. Kang, I.C. Hwang, H. Kim, K.B. Yoon, Y.S. Kang, Manual assembly of nanocrystals for enhanced photoelectrochemical efficiency of hematite film, Chem. Commun. 51 (2015) 6407–10. https://doi.org/10.1039/C5CC00200A
36. A.M. Faramawy, Hamada Elsayed, H.M. Elsayed, A.A. Sattar, Y.W. Getahun, A.A. ElGendy d, H. Kahil, Unveiling the effect of Gd3+ doping on enriching the structural, magnetic,optical, and dielectric properties of biocompatible hematite nanoparticles, J. Alloys Compd. 974 (2024) 172845
37. Hao, L. *et al.* Carbonaceous electrode materials for supercapacitors. *Adv. Mater.* **25,** 3899–3904 (2013)
38. RamachandranBalaji, Suneel Kumar, KumbamLingeshwar Reddy, Vipul Sharma, Kaustava Bhattacharyya, Venkata Krishnan, Near-infrared driven photocatalytic performance of lanthanide-dopedNaYF4@CdS core-shell nanostructures with enhanced upconversionproperties, Journal of Alloys and Compounds 724 (2017) 481-491.
39. JothirmayananthamPichaandi,Gautom Kumar Das, Noah J.J. Johnson, Tom Regier, and Frank C.J.M. van Veggel, Probing the Structure of $NaYF_4$Nanocrystals using SynchrotronBased Energy-Dependent X-ray Photoelectron Spectroscopy, J. Phys. Chem. C 2014, 118, 21639−21646.
40. Saud Khashan, SawsanDagher, Nacir Tit, AnasAlazzam, IhabObaidat, Novel method for synthesis of Fe_3O_4@TiO_2 core/shell nanoparticles, Surface & Coatings Technol. 322 (2017) 92–98. https://doi.org/10.1016/j.surfcoat.2017.05.045
41. A.K. Shimi, C. Parvathiraj, S. Kumari, J. Dalal, V. Kumar, S.M. Wabaidur, Z.A. Alothman, Green synthesis of SrO nanoparticles using leaf extract of Albiziajulibrissin and its recyclable photocatalytic activity: an eco-friendly approach fortreatment of industrial wastewater, Environ. Sci. Adv. 1 (2022) 849–861.
42. S. Sivakumar, L. Nelson Prabu, Enhancement in electrochemical behavior of cobalt doped α-MnO_2 nanoparticles, Inorgan. Chem. Commun. 147 (2023) 110247. https://doi.org/10.1016/j.inoche.2022.110247

43. G.S. Gund, D.P. Dubal, D.S. Dhawale, S.S. Shinde, C.D. Lokhande, Porous CuO nanosheet clusters prepared by a surfactant assisted hydrothermal method for high performance supercapacitors, RSC Adv., 3 (2013), pp. 24099-24107, 10.1039/C3RA43254H
44. J. Li, Y. Ren, S. Wang, Z. Ren, J. Yu, Transition metal doped MnO_2nanosheets grown on internal surface of macroporous carbon for supercapacitors and oxygen reduction reaction electrocatalysts, Appl. Mater. Today, 3 (2016) 63–72. https://doi.org/10.1016/j.apmt.2016.03.003
45. Xuechun Xiao, Bingqian Han, Gang Chen, Lihong Wang, Yude Wang, Preparation and electrochemicalperformances of carbon sphere@ZnO core-shell nanocomposites for supercapacitor applications, Scientific RepoRts, 7 (2017) 40167. DOI: 10.1038/srep40167.
46. Ahlam Albeladi, Zaheer Khan, Shaeel Ahmed Al-Thabaiti, Rajan Patel, Maqsood Ahmad Malik Shilpa Mehta, Fe_3O_4-CdO Nanocomposite for Organic Dye Photocatalytic Degradation: Synthesis and Characterization, *Catalysts* 2024, 14(1), 71.